nature astronomy

LETTERS

https://doi.org/10.1038/s41550-020-1143-y

Check for updates

Demonstration of stellar intensity interferometry with the four VERITAS telescopes

A. U. Abeysekara[1], W. Benbow[2], A. Brill[3], J. H. Buckley[4], J. L. Christiansen[5], A. J. Chromey[6], M. K. Daniel[2], J. Davis[1], A. Falcone[7], Q. Feng[8], J. P. Finley[9], L. Fortson[10], A. Furniss[11], A. Gent[12], C. Giuri[13], O. Gueta[13], D. Hanna[14], T. Hassan[13], O. Hervet[15], J. Holder[16], G. Hughes[2], T. B. Humensky[3], P. Kaaret[17], M. Kertzman[18], D. Kieda[1]✉, F. Krennrich[6], S. Kumar[14], T. LeBohec[1], T. T. Y. Lin[14], M. Lundy[14], G. Maier[13], N. Matthews[1]✉, P. Moriarty[19], R. Mukherjee[8], M. Nievas-Rosillo[13], S. O'Brien[14], R. A. Ong[20], A. N. Otte[12], K. Pfrang[13], M. Pohl[13,21], R. R. Prado[13], E. Pueschel[13], J. Quinn[22], K. Ragan[14], P. T. Reynolds[23], D. Ribeiro[3], G. T. Richards[16], E. Roache[2], J. L. Ryan[20], M. Santander[24], G. H. Sembroski[9], S. P. Wakely[25], A. Weinstein[6], P. Wilcox[10], D. A. Williams[15] and T. J. Williamson[16]

High angular resolution observations at optical wavelengths provide valuable insights into stellar astrophysics[1,2], and enable direct measurements of fundamental stellar parameters[3,4] and the probing of stellar atmospheres, circumstellar disks[5], the elongation of rapidly rotating stars[6] and the pulsations of Cepheid variable stars[7]. The angular size of most stars is of the order of one milliarcsecond or less, and to spatially resolve stellar disks and features at this scale requires an optical interferometer using an array of telescopes with baselines on the order of hundreds of metres. We report on the implementation of a stellar intensity interferometry system developed for the four VERITAS imaging atmospheric Cherenkov telescopes. The system was used to measure the angular diameter of the two sub-milliarcsecond stars β Canis Majoris and ϵ Orionis with a precision of greater than 5%. The system uses an offline approach in which starlight intensity fluctuations that are recorded at each telescope are correlated post observation. The technique can be readily scaled onto tens to hundreds of telescopes, providing a capability that has proven technically challenging to the current generation of optical amplitude interferometry observatories. This work demonstrates the feasibility of performing astrophysical measurements using imaging atmospheric Cherenkov telescope arrays as intensity interferometers and shows the promise for integrating an intensity interferometry system within future observatories such as the Cherenkov Telescope Array.

High angular resolution optical astronomy is often performed through optical amplitude interferometry (OAI), which measures the source spatial coherence function by observing the fringe visibility of interference patterns produced by the superposition of light collected at separated telescopes[8]. Another approach is stellar intensity interferometry (SII), which uses instead correlations of starlight intensity fluctuations recorded with independent detectors on separated telescopes to measure the spatial coherence[9]. SII was developed in the late 1950s[10] and resulted in the Narrabri Stellar Intensity Interferometer (NSII). The NSII was used for observations from 1963 to 1974 and provided the first definitive catalogue of 32 stellar angular diameters[11]. Observations with the NSII were limited to only very bright stars with visual magnitudes of less than 2.5. The sensitivity of an SII telescope is linearly proportional to the telescope area and detector efficiency, and is inversely proportional to the square root of the time resolution, as shown in the Methods section (see equation (6)). The capabilities of the NSII were restricted by these factors, and concurrent technical advancements in OAI provided substantial gains in the achievable limiting magnitude with much smaller telescopes, forestalling developments in astronomical SII efforts.

[1]Department of Physics and Astronomy, University of Utah, Salt Lake City, UT, USA. [2] Center for Astrophysics | Harvard & Smithsonian, Cambridge, MA, USA. [3]Physics Department, Columbia University, New York, NY, USA. [4]Department of Physics, Washington University, St. Louis, MO, USA. [5]Physics Department, California Polytechnic State University, San Luis Obispo, CA, USA. [6]Department of Physics and Astronomy, Iowa State University, Ames, IA, USA. [7]Department of Astronomy and Astrophysics, Pennsylvania State University, University Park, PA, USA. [8]Department of Physics and Astronomy, Barnard College and Columbia University, New York, NY, USA. [9]Department of Physics and Astronomy, Purdue University, West Lafayette, IN, USA. [10]School of Physics and Astronomy, University of Minnesota, Minneapolis, MN, USA. [11]Department of Physics, California State University–East Bay, Hayward, CA, USA. [12]School of Physics and Center for Relativistic Astrophysics, Georgia Institute of Technology, Atlanta, GA, USA. [13]DESY, Zeuthen, Germany. [14]Physics Department, McGill University, Montreal, Quebec, Canada. [15]Santa Cruz Institute for Particle Physics and Department of Physics, University of California, Santa Cruz, CA, USA. [16]Department of Physics and Astronomy and the Bartol Research Institute, University of Delaware, Newark, DE, USA. [17]Department of Physics and Astronomy, University of Iowa, Iowa City, IA, USA. [18]Department of Physics and Astronomy, DePauw University, Greencastle, IN, USA. [19]School of Physics, National University of Ireland, Galway, Galway, Ireland. [20]Department of Physics and Astronomy, University of California, Los Angeles, CA, USA. [21]Institute of Physics and Astronomy, University of Potsdam, Potsdam-Golm, Germany. [22]School of Physics, University College Dublin, Dublin, Ireland. [23]Department of Physical Sciences, Cork Institute of Technology, Cork, Ireland. [24]Department of Physics and Astronomy, University of Alabama, Tuscaloosa, AL, USA. [25]Enrico Fermi Institute, University of Chicago, Chicago, IL, USA. ✉e-mail: dave.kieda@physics.utah.edu; nolankmatthews@gmail.com

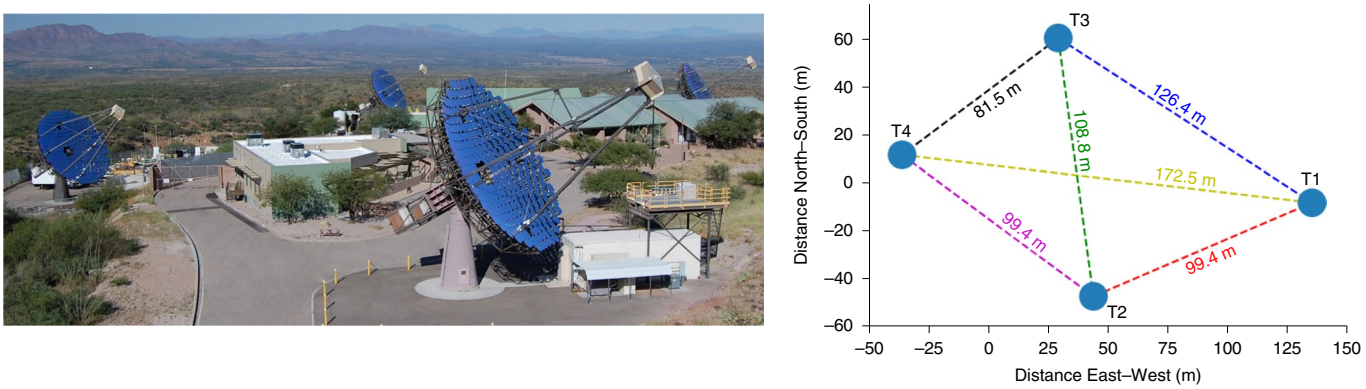

Fig. 1 | The VERITAS array. Left, Photograph of VERITAS located at the Fred Lawrence Whipple Observatory located in Amado, Arizona, USA. The array consists of four 12-m diameter telescopes, T1 (front centre), T2 (leftmost), T3 (rightmost) and T4 (back centre). The right plot shows a top-down view of the array with each of the radial telescope separations.

SII has re-emerged as a viable technique for high angular resolution astronomy, primarily owing to the potential of outfitting current and future large diameter (>10 m) telescope arrays with SII capabilities[12,13]. A suitable SII instrument must record the starlight intensity with nanosecond-level time resolution and then correlate the intensities between telescope pairs. The optical path length only need be known to a level of a few centimetres, where the required precision is determined by the light travel distance over a duration equal to the detector time resolution. The insensitivity to optical imperfections allows for SII instrumentation to be installed onto imaging atmospheric Cherenkov telescope (IACT) arrays constructed for gamma-ray astronomy. IACTs are among the largest astronomical light collectors, with mirror diameters that typically exceed 10 m. They employ fast (f ~ 1.0) optics with segmented mirrors to reduce cost, and so the large light collection area is achieved at the expense of imaging resolution. But they remain capable of performing rapid optical photometry[14] and making SII measurements of stars that are several magnitudes fainter than those accessible to the NSII[15]. There are several practical features of a modern SII observatory that uniquely complement the current capabilities of OAI. The tolerance to path length fluctuations makes possible observations at all optical wavelengths, even in the U and B photometric bands that are generally inaccessible to OAI observatories on account of the required mechanical precision at a fraction of a wavelength. Furthermore, the baselines between telescopes can be made arbitrarily large to probe unprecedented angular scales as small as tens of microarcseconds with kilometre-length baselines. A notable advantage of SII is that the technique can be scaled up to an arbitrary number of telescopes, as only digital electronic connections are required[16], enabling an optical intensity interferometry observatory that operates in a way that is comparable to radio interferometry. These realizations have led to several recent experimental efforts towards the development of a modern intensity interferometer[17–20], successful SII observations of coherent intensity fluctuations using two telescopes[21,22], and distance calibration to the luminous blue variable P Cygni[23]. We improve upon these observations by directly measuring angular stellar diameters using fits to the squared visibility–baseline dependence, with an SII system extended to four telescopes to provide six simultaneous baselines.

Here, we report on observations of the two bright ($m_V < 2.1$), hot ($T_{eff} > 22{,}000$ K) B stars ϵ Orionis (Alnilam) and β Canis Majoris (Mirzam) that were conducted using an SII system (see Methods) installed onto the Very Energetic Radiation Imaging Telescope Array System (VERITAS) IACTs shown in Fig. 1 (ref. [24]). A total of 4.25 and 5.5 h of data were collected for ϵ Ori and β CMa, respectively, spanning the nights of 2019 December 12–14, local time. The interferometric (u,v)-plane coverage[25] for each source is shown in Extended Data Fig. 1. The observations took place within a few days of the full moon when VERITAS does not operate as a gamma-ray instrument, as the night sky background light overwhelms the faint Cherenkov signal. A custom camera is mounted near the focal plane of the VERITAS telescopes, directly in front of the gamma-ray camera, to enable SII observations. The starlight is passed through an interferometric filter with an effective centre wavelength of $\lambda = 416$ nm and a bandpass of $\Delta\lambda = 13$ nm that were chosen to match the peak reflectivity and quantum efficiency of the mirrors and detector. The filtered starlight is then detected by a photomultiplier tube. The resulting signal is continuously digitized and streamed to disk at a rate of 250 mega samples per second (MS s^{-1}) at each telescope. Correlations between the intensities recorded at each telescope are performed offline using a field-programmable gate array. Then, we correct the correlated data for instrumental and geometrical time delays and for background light effects, and apply noise cuts, to obtain the squared first-order coherence function $|g^{(1)}(\tau, r)|^2$ that is proportional to the squared visibility measured in OAI. It is a function of the path delay corrected time lag τ and projected baseline $\boldsymbol{r}$ that is defined as the separation between the telescopes as viewed from the star. As the star tracks through the sky, a given telescope pair will span a range of projected baselines. The amplitude of $|g^{(1)}(r)|^2$ at $\tau = 0$ measures the spatial coherence that is dependent on the source angular brightness distribution and the projected baseline, and it reaches a minimum at the baseline $r \sim 1.22\lambda\,\theta^{-1}$ for an observation wavelength λ and stellar angular diameter θ. The angular diameter can then be determined by fitting the $|g^{(1)}(r)|^2$ measurements to an appropriate visibility model for a given source angular brightness distribution (see the Analysis section for more details). Stars that have a larger angular diameter will show a more rapid decline in $|g^{(1)}(r)|^2$ compared to stars with smaller angular diameters.

Figure 2 presents the temporal and spatial correlation measurements from the observations of β CMa and ϵ Ori. In it are shown the integrated $|g^{(1)}(\tau)|^2$ correlations for various pairs of the telescopes as a function of τ. The peak at $\tau = 0$ is the signal associated with the spatial coherence of the star. The width of the $|g^{(1)}(\tau)|^2$ peak is determined by the correlation between the combined telescope optics and detector time response at each telescope. The dashed lines show Gaussian fits to the data. The Gaussian fit width, representative of the temporal resolution time of the system, is fixed to 4 ns, as explained in the Methods, and the amplitude is left as a free parameter. Values of $|g_*^{(1)}(r)|^2$ represent the correlation resulting only from starlight (Fig. 2, bottom panels). These values are obtained by scaling the $|g^{(1)}(\tau, r)|^2$ amplitude fit by a factor that

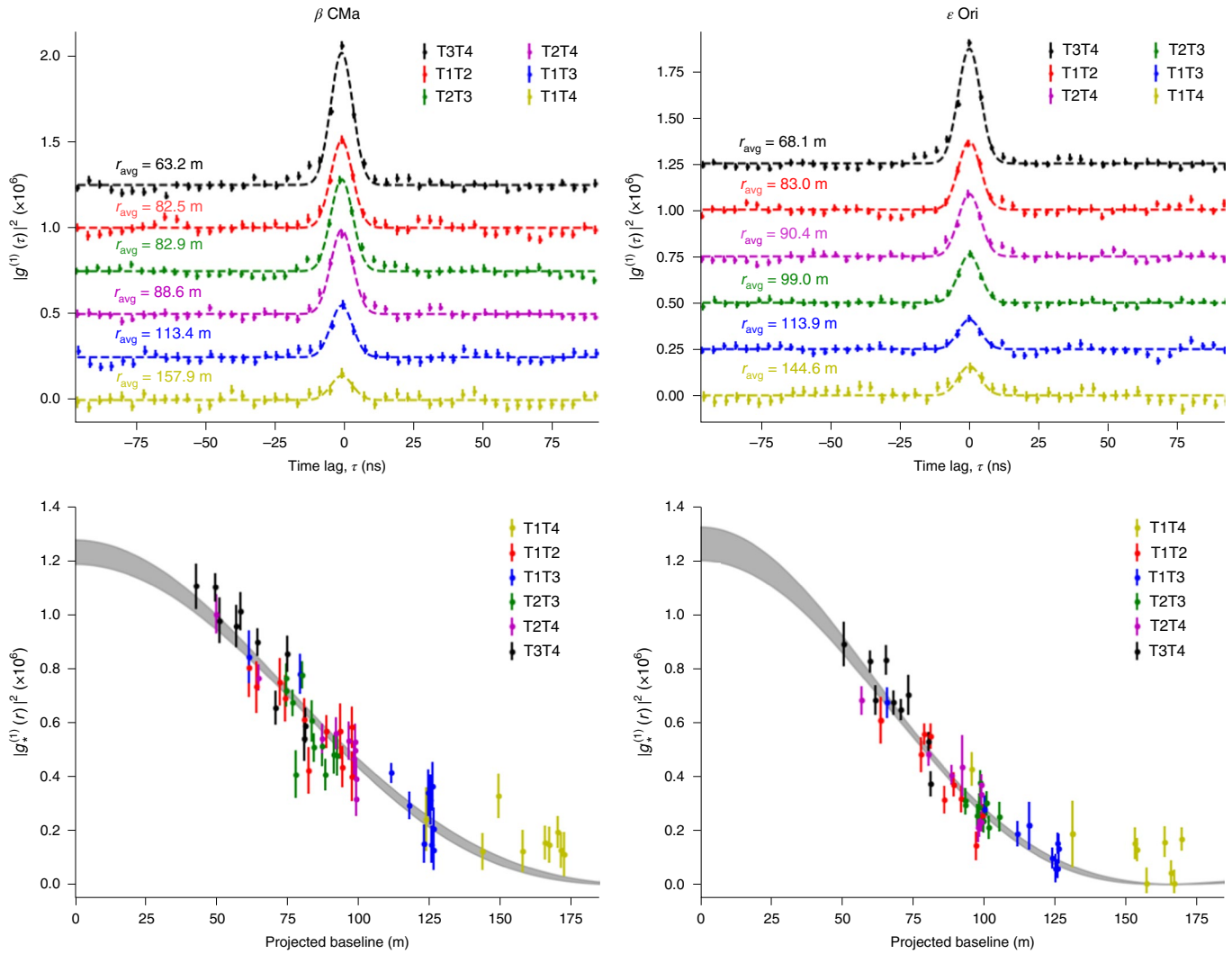

Fig. 2 | Temporal and spatial coherence measurements. The top two panels show the averaged $|g^{(1)}(\tau)|^2$ correlation measurements over the full live time between different pairs of telescopes for β CMa (left) and ϵ Ori (right). Each telescope pair measurement is colour coded to match the combinations shown in Fig. 1. The uncertainties are given by the standard deviation of the mean normalized correlation and are estimated independently for each time lag. The correlations are ordered by increasing average baseline from the top, corresponding to decreasing spatial coherence. The dashed lines show Gaussian fits to the data. The amplitude and corresponding fit uncertainty of the $|g^{(1)}(\tau)|^2$ peak over shorter time intervals are obtained as a function of the baseline and shown by the individual points in the bottom panels. The uncertainty is determined by the square root of the covariance matrix resulting from the fit. These measurements are fit to a function that approximates the star as a uniform disk (see equation (3)) and includes free parameters for the overall normalization and angular diameter. The shaded area shows the 68% confidence intervals determined through the uncertainties in the fit parameters.

accounts for the effects of night sky background light and detector dark current. Each set of points is shown as a function of the projected baseline and corresponds to an average of 17 min. of data live time per measurement. The live time is defined as the resulting exposure after noise cuts are applied. Using uniform-disk and limb-darkened models for the star angular brightness distribution, we perform a fit to the data with the stellar diameter and the zero-baseline correlation as free parameters. The shaded region shows the 68% confidence regions obtained from the uniform-disk fit. The value of the zero-baseline correlation should be on the order of the ratio of the electronic to the optical bandwidth, each set by the instrumental system. In practice, the measured correlation can be affected by other factors, including the telescope mirror extent and spectral absorption or emission lines. We find that these additional effects are negligible in comparison to our measurement uncertainty, and therefore the zero-baseline value should be the same for both stars. The zero-baseline normalization fit values are measured to be $N_0 = (1.23 \pm 0.05) \times 10^{-6}$ for β CMa and $N_0 = (1.26 \pm 0.06) \times 10^{-6}$ for ϵ Ori and are consistent within fitted errors, which demonstrates that the system is robust to systematic effects in observations of different stars.

For β CMa, we find a uniform-disk diameter of $\theta_{UD} = 0.523 \pm 0.017$ mas, in agreement with the original NSII measurement of $\theta_{UD} = 0.50 \pm 0.03$ mas (ref. [11]). In the case of ϵ Ori, we obtain $\theta_{UD} = 0.631 \pm 0.017$ mas, also in agreement with the NSII measurements ($\theta_{UD} = 0.67 \pm 0.04$ mas). Using a limb-darkened model, given by equation (4) (Methods), we find limb-darkened diameters of $\theta_{LD} = 0.542 \pm 0.018$ mas for β CMa and $\theta_{LD} = 0.660 \pm 0.018$ mas for ϵ Ori. We note that the VERITAS stellar intensity interferometer (VSII) gave more precise angular diameter measurements than the NSII, in less than

one-tenth of the observation time. The improvement is largely due to the greater light collection areas of the VERITAS mirrors, as well as the increased instantaneous baseline coverage offered by using multiple telescopes. To our knowledge, no angular diameter measurements of these stars have been made since those using the NSII. Therefore, the current work provides confirmation of the NSII measurements of the stellar angular diameters to a certainty of more than 95%, which is a requirement for many science topics described later. Future observations can further reduce the uncertainty, as the root mean square fluctuations in the correlation should reduce inversely with the square root of the observation time. Here, we measure the uncertainty of the $|g^{(1)}(\tau)|^2$ fluctuations at a level of 2.0×10^{-8} for several telescope pairs using the entire data set for ϵ Ori. This value corresponds to an uncertainty in the squared visibility of 1.6% for the measured zero-baseline correlation of $N_0 = 1.26 \times 10^{-6}$. The extrapolation of these results to fainter stars demonstrates the current capability to measure squared visibilities with a precision of 4.0% for stars of magnitude 2.5, and 10% for stars with magnitude 3.5 for an equivalent observation time. Direct comparison of these results with those from the NSII (ref. [11]) shows an improvement in the sensitivity by a factor of 6. Future improvements in the duty cycle and collimation of light through the narrowband filter offer expected gains in the sensitivity by a factor of 2 to 3, and therefore offer the potential for optical intensity interferometry measurements of stars with $m_B \sim 5$.

These two stellar angular diameter measurements with VSII demonstrate the feasibility of performing optical interferometry with IACT arrays. The approach developed here using high-speed streaming with offline correlations demonstrates the technical capability to perform optical intensity interferometry with tens to hundreds of telescopes, a capability that remains challenging for modern OAI observatories. We also show that SII observations increase the scientific output and scope of IACT observatories during bright moonlight conditions when gamma-ray observations are otherwise limited. The future Cherenkov Telescope Array (CTA) will use up to 99 telescopes with baselines of up to a kilometre in length in the Southern Hemisphere, and 19 telescopes in the Northern Hemisphere with baselines of up to several hundred metres[26], and will allow for unprecedented angular resolution capabilities approaching the scale of tens of microarcseconds. The large number of telescopes would provide hundreds and possibly thousands of simultaneous baselines. Capability studies of SII on a CTA-like observatory demonstrate the ability to observe stellar targets that are as faint as $m_V \sim 6$ or 7 (ref. [27]). Scientific studies that would be made possible by a future CTA-SII observatory include surveying the angular diameter of stars larger than ~0.05 mas at short visible wavelengths, measuring the orbital and stellar parameters of interacting binaries[28], characterizing the effects of gravity darkening and rotational deformation of rapidly rotating stars[29], and imaging of dark or hot starspots[27]. The VSII observations presented here demonstrate the core requirements for such an observatory, thus providing a technological pathway in addition to performing SII observations with unprecedented sensitivity. Our experiment shows it is possible to attain squared visibilities with uncertainties of less than a few per cent and therefore that SII observations can directly complement ongoing science campaigns pursued by current OAI observatories[30].

Methods

Instrumentation. The VERITAS observatory at the Fred Lawrence Whipple Observatory, Amado, Arizona, USA, consists of an array of four 12-m diameter telescopes of the Davies–Cotton design. The primary mirror of each telescope consists of 345 hexagonal mirror facets arranged in f/1 optics. SII hardware is mounted onto an aluminium plate that is installed in front of the VERITAS gamma-ray camera. Initial tests of the hardware were performed in the laboratory[31] and with on-sky tests at the StarBase Observatory, Utah, USA[32]. The equipment was then scaled for use on the VERITAS telescopes, with successful tests of correlated intensity fluctuations with two telescopes[33]. On the plate, a 45° mirror redirects the light from the primary mirror onto an optical diaphragm with a diameter corresponding to approximately 0.1° on the sky. The light then passes through an interferometric filter (SEMROCK 420/5) with a vendor-specified centre wavelength of 420 nm and a bandpass of 5 nm. As the light is not collimated onto the filter, the effective bandpass is broadened owing to the large angle of incident light of up to 26.6°. Calculations established the resulting bandpass to be centred on a wavelength of 416 nm with an effective width of 13 nm. This effect reduces the overall spectral density throughput, and correspondingly, the signal-to-noise ratio, by approximately a factor of 2. The light is then detected by a Hamamatsu R10650 photomultiplier tube (PMT) with a quantum efficiency of ~30% at the observing wavelength[34]. The gain of the PMT is controlled by battery-powered high voltage. The exact high voltage delivered to the PMT is set by the duty cycle of a pulse-width modulator that is connected to the high voltage supply via an optical fibre[35]. The output current of the PMT is fed into a low-noise trans-impedance FEMTO HCA-200M-20K-C 200 MHz pre-amplifier. The voltage output of the pre-amplifier drives a long triaxial cable that is connected to the data acquisition system. A National Instruments (NI) NI-5761 DC-coupled analogue-to-digital (ADC) converter continuously digitizes the amplified PMT signal at 250 MS s^{-1} with 14-bit resolution per sample over a peak-to-peak voltage range of 1.23 V. Digitized values are passed to an NI PXIe-7965R module that hosts a Virtex 5 SX95T field-programmable gate array (FPGA). The FPGA is programmed to downcast the sampled value to an 8-bit integer, and to push the data through a first-in-first-out buffer and then stream them to an NI 12 TB NI-8265 RAID disk array at a data rate of 250 MB s^{-1} per telescope. The ADC sample clock for each telescope is referenced and phase locked to a common external 10 MHz clock. To generate the reference clock, a centrally located Seven Solutions White Rabbit (WR) switch is used to distribute a 10 MHz clock through optical fibre connections to a WR-Len module located near each of the data acquisition systems. The WR-Len module takes in the optical fibre signal and generates the electronic 10 MHz signal to which the ADC sample clock is referenced.

After observations are completed, the correlation between the stored data of each telescope is processed offline by a FPGA-based correlator. The FPGA is programmed to retrieve the mean intensities of each time stream $\langle I \rangle = \frac{1}{N}\sum_i^N I(t_i)$, for the sample i, and the cross correlation between each pair of data streams, $c(k) = \langle I_1(t_i) I_2(t_{i+k}) \rangle = \frac{1}{N}\sum_i^N I_1(t_i) I_2(t_{i+k})$, where k is a digital time lag inserted between the two channels. The correlation is calculated over 64 time-lag channels, corresponding to time lags of −128 to +124 ns in steps of 4 ns.

Analysis. From the outputs of the correlator, the second-order coherence function can be calculated by normalizing the cross correlation by the product of the mean intensities,

$$g^{(2)}(\tau, r) = \frac{\langle I_1(t) I_2(r, t+\tau) \rangle}{\langle I_1(t) \rangle \langle I_2(t) \rangle} \quad (1)$$

where r is the projected baseline between the two telescopes, τ is the relative time lag and the brackets indicate a statistical average in time assuming a stationary light source. For chaotic thermal light, such as that from a star, the second-order coherence function can be written[36] in terms of the first-order coherence $g^{(1)}(\tau, r)$,

$$g^{(2)}(\tau, r) = 1 + |g^{(1)}(\tau, r)|^2 \quad (2)$$

The van Cittert–Zernike theorem states that at $\tau = 0$, the measured first-order coherence is equivalent to the Fourier transform of the source angular intensity distribution in the sky[37]. For randomly polarized light, the squared modulus of the first-order coherence is reduced by a factor of two. In the typical case in which the detector resolution time T is much longer than the light coherence time $\tau_c \sim 1/\Delta\nu$, where $\Delta\nu$ is the optical bandwidth, it is reduced by another factor of $\sim\tau_c/T$. We then write the expected zero-baseline coherence as $N_0 = \epsilon\tau_c/2T$, where ϵ is a correction factor that accounts for the shape of the detected light spectral density that sets the optical bandwidth and corresponding coherence time. The correction factor also includes potential losses in the coherence signal that are attributed to non-ideal properties of the filters, detectors and electronic readout system that may influence the effective electronic or optical bandwidth, as detailed in ref. [10]. Under a uniform-disk approximation for a star of angular diameter θ_{UD}, the squared first-order coherence can be written as

$$|g_\star^{(1)}(\tau = 0, r)|^2 = N_0 \left| 2\frac{J_1(x_{UD})}{x_{UD}} \right|^2 \quad (3)$$

where $x_{UD} = \pi\theta_{UD} r/\lambda$, $|g_\star^{(1)}|^2$ is the coherence due to starlight alone; that is, $g_\star^{(2)} = \langle I_{1,\star} I_{2,\star} \rangle / (\langle I_{1,\star} \rangle \langle I_{2,\star} \rangle)$, where $I_{1,\star}$ and $I_{2,\star}$ are the starlight intensities at detectors 1 and 2, J_1 is the Bessel function of the first kind, and λ is the mean observational wavelength. A linear limb-darkened model[38] was also fit to the data, where the expected squared first-order coherence is given by

$$|g_\star^{(1)}(\tau = 0, r)|^2 = N_0 \left(\frac{1-u_\lambda}{2} + \frac{u_\lambda}{3} \right)^{-2} \left((1-u_\lambda)\frac{J_1(x_{LD})}{x_{LD}} + u_\lambda \sqrt{\pi/2}\frac{J_{3/2}(x_{LD})}{x_{LD}^{3/2}} \right)^2 \quad (4)$$

where u_λ is the wavelength-dependent linear limb-darkening coefficient, and $x_{LD} = \pi\theta_{LD} r/\lambda$, where θ_{LD} is the limb-darkened angular diameter.

Table 1 | Atmospheric parameters used to estimate values of the linear limb-darkening coefficient

Source	Spectral type	B	$T_{\rm eff}$ (K)	log (g) (dex)	v sin (i) (km s^{-1})
β CMa	BII/III	1.73	24,000 ± 500[a]	3.43 ± 0.10[a]	20 ± 7[a]
ϵ Ori	B0Ia	1.51	27,000 ± 1,000[b]	2.90 ± 0.02[b]	65 ± 15[c]

The spectral type and B-band magnitudes were obtained from SIMBAD (http://simbad.u-strasbg.fr/simbad/). [a]Taken from ref. [41]. [b]Taken from ref. [42]. [c]Taken from ref. [43].

The measured spatial coherence signal can be affected by detector dark current and background light. The total signal intensity can be written as a sum of the starlight and background light sources, $I(t) = I_\star + I_{\rm bkg}$, and using equation (1) it is straightforward to derive the relationship

$$|g^{(1)}_\star|^2 = |g^{(1)}|^2 \times (1+\beta_1)(1+\beta_2) \quad (5)$$

under the assumption that the fluctuations in the starlight background and the dark current background terms are uncorrelated (that is, $\langle \Delta I_1 . \Delta I_{2_{\rm bkg}} \rangle = \langle \Delta I_{1_{\rm bkg}} \Delta I_{2_\star} \rangle = \langle \Delta I_{1_{\rm bkg}} \Delta I_{2_{\rm bkg}} \rangle = 0$, where ΔI is the fluctuating component of the given source intensity such that $I(t) = \langle I \rangle + \Delta I(t)$). The terms β_1 and β_2 are the ratios of the background to starlight intensity $I_{\rm bkg}/I_\star$ for a given telescope.

The expected signal-to-noise ratio of the correlation due to the spatial coherence of the source, under a first-order approximation, is given as

$$S/N = A\,\alpha\,n|g^{(1)}(r)|^2\sqrt{\frac{\Delta f T_0}{2}} \quad (6)$$

where A is the telescope mirror area, α is the quantum efficiency of the detectors, n is the spectral flux density of the source given in units of photons s^{-1} m^{-2} Hz^{-1}, Δf is the electronic bandwidth set by the time response of the combined optical and electronic system, and T_0 is the observation duration[9].

For a given run, typically 20 to 30 min. in duration, the value of $|g^{(1)}(\tau)|^2$ is calculated over accumulation frames of 1 s. Any $|g^{(1)}(\tau)|^2$ frames contaminated by correlated high-frequency radio pickup are removed. The Fourier transform of each frame is calculated to identify corrupted frames. If the power at the specific noise frequency is greater than the average power over all other frequencies by a predetermined threshold cut, the frame is removed. For a typical run, 30–40% of the data are removed as a result of the electronic noise. In addition, any frames in which the mean PMT current falls below 5 μA, or approximately one-half of the total current due to starlight, are removed. These current losses are attributed to the attenuation of starlight by clouds, or the loss of starlight not centred onto the detectors due to imperfect telescope tracking. Each frame is shifted in time by the average number of samples to zero optical path delay to correct for the geometrical optical path delay. After path-delay corrections and the application of noise and current cuts, all $|g^{(1)}(\tau)|^2$ frames are averaged together through a weighted mean to produce a final $|g^{(1)}(\tau)|^2$ frame for that run. The weights for each frame are given by $1/\sigma^2_{|g^{(1)}|^2}$, where $\sigma_{|g^{(1)}|^2} = \sigma_{\langle I_1 I_2 \rangle}/(\langle I_1 \rangle \langle I_2 \rangle)$, and $\sigma_{\langle I_1 I_2 \rangle}$ is the standard deviation of the correlation over all time-lag bins for a given frame. Provided sufficient throughput and spatial coherence, the corrected and averaged results reveal an excess peak at zero time lag due to the spatial coherence of the source. In this study, the detector resolution time is much greater than the coherence time of the light, and therefore the shape of the peak is determined by the cross correlation of the telescope and detector time response, with an amplitude proportional to the amount of spatial coherence. The Davies–Cotton mirror design of the VERITAS telescopes introduces an approximate 4 ns spread in the arrival time of photons that otherwise would arrive synchronously[39]. A PMT detects the photons with a characteristic single photo-electron pulse width of 3.7 ns and additional timing jitter on the order of 1 ns. Simulations of these effects find that the $|g^{(1)}(\tau)|^2$ peak can be modelled as a Gaussian following the form

$$f(\tau) = Ae^{-\frac{1}{2}(\tau-\tau_0)^2/\sigma_\tau^2} + C \quad (7)$$

with A, τ_0 and C left as fit parameters. A is the amplitude of the coherence peak and directly measures $|g^{(1)}(r)|^2$, τ_0 is a parameter that accounts for a variable start time between the separated data acquisition systems, and is constrained within $|\tau| < 10$ ns of zero lag, and C is another correction parameter that subtracts any drift in the mean level of the correlator. The value of the fit width is fixed to a value of $\sigma_\tau = 4.0$ ns, which was determined empirically from the data and is consistent with expectations from simulations. The value of the width was obtained by allowing it to be a free parameter in the fit of the integrated $|g^{(1)}(\tau)|^2$ correlation measurements for runs showing a peak amplitude with a P value less than 3×10^{-7}. The value of the fit width was stable within fit uncertainties for several runs, demonstrating that no statistically significant fluctuations in the relative timing of the acquisition systems are present.

The value of the fit amplitude and corresponding uncertainty are found for all runs to measure $|g^{(1)}(\tau = 0)|^2$ as a function of the projected baseline. The projected baseline is calculated from the telescope positions and source sky position at the time of observation. The value of the fit amplitude is then multiplied by the scaling factor described in equation (5) to compensate for night sky background and detector dark current. The mean level of the background is found by pointing the telescope off source and recording the average intensity. These off runs are taken before and after each run on source. The background-light corrected values of $|g^{(1)}_\star|^2$ are then fit to a function with the form of equation (3) to obtain the uniform-disk normalization and stellar diameter. Values of the linear limb-darkening coefficient u_λ were estimated by interpolating existing tables that calculate expected values of u_λ from atmospheric parameters[40]. Using the atmospheric values listed in Table 1 for observations in the B band, a microturbulent velocity of 2 km s^{-1} and solar metallicity, we find values of u_λ of 0.38 and 0.46 for β CMa and ϵ Ori, respectively.

Data availability

The data that support the plots within this paper and other findings of this study are available from the corresponding authors upon reasonable request. Given the extremely large datasets obtained during the observations, in excess of 40 TB, only the post-correlation data can be reasonably made available.

Code availability

The software used to analyse the data in this study is available upon request to the corresponding authors.

Received: 27 February 2020; Accepted: 2 June 2020;
Published online: 20 July 2020

References

1. Monnier, J. Optical interferometry in astronomy. *Rep. Prog. Phys.* **66**, 789–857 (2003).
2. Ridgway, S. et al. Revitalizing the optical/infrared interferometry community in the U.S. *Bull. Am. Astron. Soc.* **51**, 157 (2019).
3. Boyajian, T. S. et al. Stellar diameters and temperatures. III. Main-sequence A, F, G, and K stars: additional high-precision measurements and empirical relations. *Astrophys. J.* **771**, 40 (2013).
4. Casagrande, L. et al. Towards stellar effective temperatures and diameters at 1 per cent accuracy for future surveys. *Mon. Not. R. Astron. Soc.* **439**, 2060–2073 (2014).
5. Kraus, S. et al. Gas distribution, kinematics, and excitation structure in the disks around the classical Be stars β Canis Minoris and ζ Tauri. *Astrophys. J.* **744**, 19 (2012).
6. van Belle, G. T. Interferometric observations of rapidly rotating stars. *Astron. Astrophys. Rev.* **20**, 51 (2012).
7. Kervella, P. et al. Observational calibration of the projection factor of Cepheids: III. The long-period Galactic Cepheid RS Puppis. *Astron. Astrophys.* **600**, A127 (2017).
8. Labeyrie, A., Lipson, S. G. & Nisenson, P. *An Introduction to Optical Stellar Interferometry* (Cambridge Univ. Press, 2006).
9. Hanbury Brown, R. & Twiss, R. Q. Interferometry of the intensity fluctuations in light. Part I. Basic theory: the correlation between photons in coherent beams of radiation. *Proc. R. Soc. Ser. A* **242**, 300–324 (1957).
10. Hanbury Brown, R. *The Intensity Interferometer; its applications to astronomy* (Taylor & Francis, 1974).
11. Hanbury Brown, R., Davis, J. & Allen, L. R. The angular diameters of 32 stars. *Mon. Not. R. Astron. Soc.* **167**, 121–136 (1974).
12. LeBohec, S. & Holder, J. Optical intensity interferometry with atmospheric Cerenkov telescope arrays. *Astrophys. J.* **649**, 399–405 (2006).
13. Pilyavsky, G. et al. Single-photon intensity interferometry (SPIIFy): utilizing available telescopes. *Mon. Not. R. Astron. Soc.* **467**, 3048–3055 (2017).
14. Lacki, B. C. Cherenkov telescopes as optical telescopes for bright sources: today's specialized 30-m telescopes? *Mon. Not. R. Astron. Soc.* **416**, 3075–3082 (2011).
15. Rou, J., Nuñez, P. D., Kieda, D. & LeBohec, S. Monte Carlo simulation of stellar intensity interferometry. *Mon. Not. R. Astron. Soc.* **430**, 3187–3195 (2013).
16. Dravins, D., Lagadec, T. & Nuñez, P. Optical aperture synthesis with electronically connected telescopes. *Nat. Commun.* **6**, 6852 (2015).
17. Weiss, S. A., Rupert, J. D. & Horch, E. P. Stellar photon correlation detection with the Southern Connecticut stellar interferometer. In *Optical and Infrared Interferometry and Imaging VI, Proc. SPIE* Vol. 10701 (eds Creech-Eakman, M. J., et al.), 107010X (2018).
18. Zampieri, L. et al. Intensity interferometry with Aqueye+ and Iqueye in Asiago. In *Optical and Infrared Interferometry and Imaging V, Proc. SPIE* Vol. 9907 (eds Malbet, F. et al.), 99070N (2016).
19. Tan, P. K., Chan, A. H. & Kurtsiefer, C. Optical intensity interferometry through atmospheric turbulence. *Mon. Not. R. Astron. Soc.* **457**, 4291–4295 (2016).

20. Zmija, A. et al. LED as laboratory test source for astronomical intensity interferometry. *Opt. Express* **28**, 5248–5256 (2020).
21. Guerin, W. et al. Spatial intensity interferometry on three bright stars. *Mon. Not. R. Astron. Soc.* **480**, 245–250 (2018).
22. Acciari, V. A. et al. Optical intensity interferometry observations using the MAGIC imaging atmospheric Cherenkov telescopes. *Mon. Not. R. Astron. Soc.* **491**, 1540–1547 (2019).
23. Rivet, J. P. et al. Intensity interferometry of P Cygni in the Hα emission line: towards distance calibration of LBV supergiant stars. *Mon. Not. R. Astron. Soc.* **494**, 218–227 (2020).
24. Kieda D., LeBohec, C. & Cardon, R. Augmentation of VERITAS telescopes for stellar intensity interferometry. In *36th International Cosmic Ray Conference*, 714 (Proceedings of Science, 2019).
25. Ségransan, D. Observability and UV coverage. *New Astron. Rev.* **51**, 597–603 (2007).
26. Acharyya, A. et al. Monte Carlo studies for the optimisation of the Cherenkov telescope array layout. *Astropart. Phys.* **111**, 35–53 (2019).
27. Nuñez, P. D., Holmes, R., Kieda, D., Rou, J. & LeBohec, S. Imaging submilliarcsecond stellar features with intensity interferometry using air Cherenkov telescope arrays. *Mon. Not. R. Astron. Soc.* **424**, 1006–1011 (2012).
28. Dravins, D., LeBohec, S., Jensen, H. & Nuñez, P. D. Optical intensity interferometry with the Cherenkov telescope array. *Astropart. Phys.* **43**, 331–347 (2013).
29. Nuñez, P. D. & Domiciano de Souza, A. Capabilities of future intensity interferometers for observing fast-rotating stars: imaging with two- and three-telescope correlations. *Mon. Not. R. Astron. Soc.* **453**, 1999–2005 (2015).
30. Stee et. al. Science cases for a visible interferometer. Preprint at https://arxiv.org/abs/1703.02395 (2017).
31. Matthews, N., Kieda, D. & LeBohec, S. Development of a digital astronomical intensity interferometer: laboratory results with thermal light. *J. Mod. Opt.* **65**, 1336–1344 (2018).
32. Matthews, N., Clarke, O., Snow, S., LeBohec S. & Kieda D. Implementation of an intensity interferometry system on the StarBase observatory. In *Optical and Infrared Interferometry and Imaging VI, Proc. SPIE* Vol. 10701 (eds Creech-Eakman, M. J., et al.), 107010W (2018).
33. Matthews, N. et. al. Astrophysical measurements with the VERITAS Stellar Intensity Interferometer. In *36th International Cosmic Ray Conference*, 740 (Proceedings of Science, 2019).
34. Otte, A. N. et. al. The upgrade of VERITAS with high efficiency photomultipliers. In *32nd International Cosmic Ray Conference*, 247 (2011).
35. Cardon, R., Matthews, N., Abeysekara, A. U. & Kieda, D. A fiber optic based high voltage system for stellar intensity interferometry observations. In *36th International Cosmic Ray Conference*, 643 (Proceedings of Science, 2019).
36. Foellmi, C. Intensity interferometry and the second-order correlation function $g^{(2)}$ in astrophysics. *Astron. Astrophys.* **507**, 1719–1727 (2009).
37. Born, M. & Wolf, E. in *Principles of Optics* Ch. 10 (Pergamon, 1980).
38. Hanbury Brown, R., Davis, J., Lake, R. J. W. & Thompson, R. J. The effects of limb darkening on measurements of angular size with an intensity interferometer. *Mon. Not. R. Astron. Soc.* **167**, 474–484 (1974).
39. Holder, J. et al. The first VERITAS telescope. *Astropart. Phys.* **25**, 391–401 (2006).
40. Claret, A. & Bloemen, S. Gravity and limb-darkening coefficients for the Kepler, CoRoT, Spitzer, *uvby*, UBVRIJHK, and Sloan photometric systems. *Astron. Astrophys.* **529**, A75 (2011).
41. Levenhagen, R. S. & Leister, N. V. Spectroscopic analysis of southern B and Be stars. *Mon. Not. R. Astron. Soc.* **371**, 252–262 (2006).
42. Crowther, P. A., Lennon, D. J. & Walborn, N. R. Physical parameters and wind properties of Galactic early B supergiants. *Astron. Astrophys.* **446**, 279–293 (2006).
43. Abt, H. A., Levato, H. & Grosso, M. Rotational velocities of B stars. *Astrophys. J.* **573**, 359–365 (2002).

Acknowledgements

This research is supported by grants from the US Department of Energy Office of Science, the US National Science Foundation and the Smithsonian Institution, by NSERC in Canada and by the Helmholtz Association in Germany. We acknowledge the excellent work of the technical support staff at the Fred Lawrence Whipple Observatory and at the collaborating institutions for their maintenance of VERITAS and assistance with integrating the SII system. The authors gratefully acknowledge support from the US National Science Foundation grant nos. AST 1806262 and PHY 0960242, and from the University of Utah for the fabrication and commissioning of the VERITAS-SII instrumentation. This work is dedicated to the memory of Paul Nuñez.

Author contributions

All authors contributed to the operation of the VERITAS telescopes and the internal review of the manuscript. N.M. and D.K. developed the SII hardware used in these observations with assistance from M.K.D. and G.H. in the integration with VERITAS; N.M. and D.K. wrote the data acquisition software; N.M. developed the FPGA correlator software; N.M. proposed the observations; N.M. and T.H. reduced and analysed the data; N.M., D.K., T.L., T.T.Y.L., D.R., Q.F., J.D., A.U.A. and A.F. took the observations; N.M. wrote the paper with guidance from T.L., M.K.D., D.K., T.H., M.P. and J.L.R.; and T.L. and D.K. provided key insights throughout this work.

Competing interests

The authors declare no competing interests.

Additional information

Extended data is available for this paper at https://doi.org/10.1038/s41550-020-1143-y.

Correspondence and requests for materials should be addressed to D.K. or N.M.

Peer review information *Nature Astronomy* thanks William Guerin and the other, anonymous, reviewer(s) for their contribution to the peer review of this work.

Reprints and permissions information is available at www.nature.com/reprints.

Publisher's note Springer Nature remains neutral with regard to jurisdictional claims in published maps and institutional affiliations.

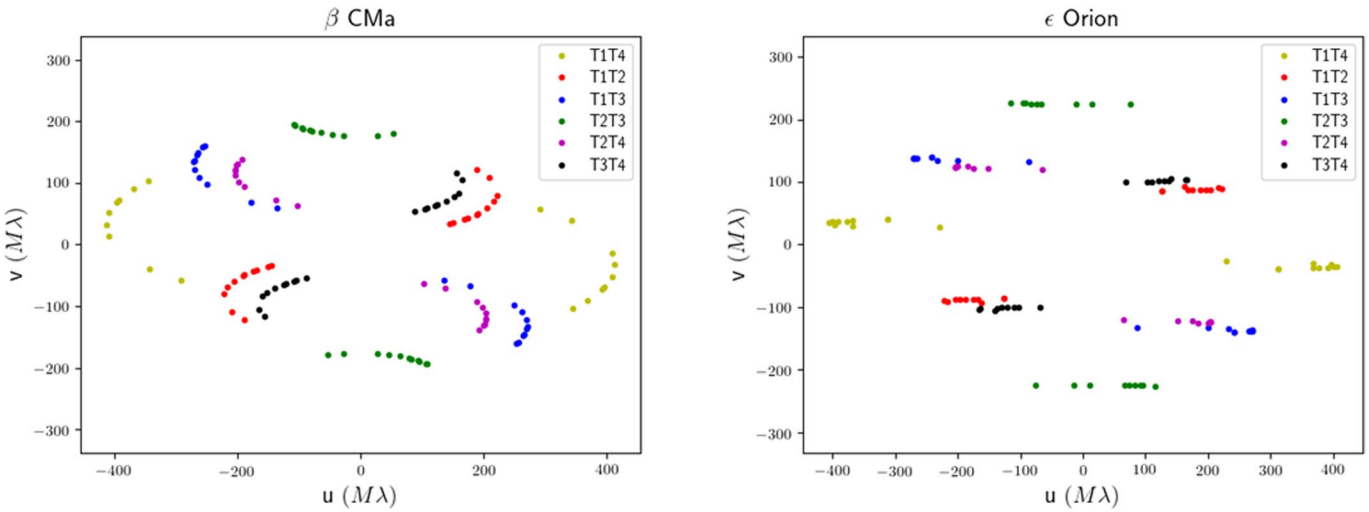

Extended Data Fig. 1 | Coverage of the sources in the (*u*, *v*)-plane. Each of the coloured points represents different runs for a given telescope pair.